Article:
Guilbaud, R, Poulton, SW orcid.org/0000-0001-7621-189X, Butterfield, NJ et al. (2 more authors) (2015) A global transition to ferruginous conditions in the early Neoproterozoic oceans. Nature Geoscience, 8 (6). pp. 466-470. ISSN 1752-0908

https://doi.org/10.1038/ngeo2434

Supplementary Information

A global transition to ferruginous conditions in the early Neoproterozoic oceans

Romain Guilbaud, Simon W. Poulton, Nicholas J. Butterfield, Maoyan Zhu, Graham A. Shields-Zhou

Geological Descriptions

Huainan region, North China craton (Fig. S1)

Nomenclatures for the North China formations are those recommended by Dong et al[1]. The Liulaobei Formation (Huainan group) is a ~700-800 m thick succession of calcareous marine mudstones intercalated with shales and siltstones that were deposited below the storm-wave base[2]. It hosts abundant acritarchs and macroscopic carbonaceous compressions[1,2]. The overlying Feishui group starts with sandstones of the Shouxian Formation (not sampled), conformably overlain by argillaceous limestones of the Jiuliqiao Formation (~50 m thick). In its lower part, the Jiuliqiao Formation consists of below storm-wave base deposits that shallow upwards towards the top of the succession. The succession yields acritarch assemblages and carbonaceous compressions similar to those present in the Liulaobei Formation[2]. The Jiuliqiao Formation is conformably overlain by the stromatolite-rich, dolomicritic Sidingshan Formation (~250 m thick). Wang et al.[3] obtained a poorly constrained whole rock Rb-Sr isochron age of 840 ± 72 Ma for the Liulaobei Formation, while possibly detrital zircons from dolerite intrusions (sills) have been dated at 976 ± 72 Ma for the Zhaowei Formation[4] (Huaibei region, stratigraphically correlated to the Jiuliqiao Formation). A less ambiguous maximum age constraint is provided by a detrital zircon U-Pb age of 1069 ± 29 Ma for the Xinxing Formation[5] (Huaibei region,

stratigraphically correlated to the Liulaobei Formation). Chemostratigraphic correlations[6] and Sr isotope data[7] also point towards a Tonian age for the Liulaobei Formation, while the presence of *Chuaria*, *Ellipsophysa* and *Tawuia* assemblages in the Liulaobei and the Jiuliqiao Formations, and of characteristic early Neoproterozoic acritarchs (*Trachyhystrichosphaera aimika*) in the Liulaobei Formation is consistent with a pre-Cryogenian age[1,2,6]. Taken together, these constraints suggest an early Neoproterozoic (early Tonian) age (~900-1000 Ma) for the succession.

Samples were collected from freshly exposed outcrops. Exceptional acritarch preservation and acritarch light colouration in the Huainan and the Huaibei regions suggest low grades of thermal maturity and little evidence for metamorphic alteration[2,6] or pervasive oxidative weathering. High Fe_{Carb} contents (55% of the highly reactive Fe on average, Table S1) suggest Fe preservation as Fe(II) and limited post-depositional sulphide oxidation. Even with partial oxidation upon exposure, Fe_{HR}/Fe_T ratios are largely preserved, and the high Fe_{HR}/Fe_T ratios throughout most of the section therefore strongly support anoxic depositional conditions. Furthermore, in the unlikely scenario of near-complete post-depositional oxidation of pyrite, but not Fe(II) in carbonates, all of the Fe released from pyrite would be present as Fe_{Ox}. Taking the worst case scenario that all of the Fe_{Ox} arises from pyrite oxidation, the anoxic samples still largely record a ferruginous, rather than euxinic, water column signal (115 samples out of 122 still record ferruginous anoxia). Such extensive pyrite oxidation would result in the presence of weathering products such as poorly crystalline Fe(III) oxides and elemental sulphur, which were never detected in our samples.

Amundsen Basin, Shaler Supergroup, arctic Canada

Amundsen basin samples encompass shallow shales closely associated with stromatolitic carbonates from the ~0.89 Ga Reynolds Point Formation, the ~0.85 Ga Wynniatt Formation and the ~0.79 Ga Kilian Formation[8]. Wynniatt macrofossils include *Chuaria* and *Tawuia* and acritarch assemblages have been described elsewhere[9].

Samples showing evidence for meteoric oxidation (such as the presence of elemental S) were not utilised for the Fe speciation. For the analysed samples, Fe_{Carb} and Fe_{Mag} represent 28% and 22% of highly reactive Fe on average (Table S1), supporting Fe preservation as a ferrous species. As with the samples from the north China craton, even if we assume extensive pyrite oxidation, recalculations of Fe_{Py}/Fe_{HR} (adding Fe_{Ox} into $Fe_{Py)}$ do not alter the dominantly ferruginous signal.

~0.81-0.79 Ga Amadeus basin, Australia

Amadeus basin samples have been collected from well-preserved drill core (Wallara-1) and are demonstrably unoxidised. They comprise shales and carbonates from the marine deposits of the Bitter Springs Formation, and marine shales from the Finke Beds. Our sample interval encapsulates the Bitter Springs $\delta^{13}C_{carb}$ negative excursion and its termination[10], and the TOC contents are of the same order of magnitude as in the Huainan section (Table S1).

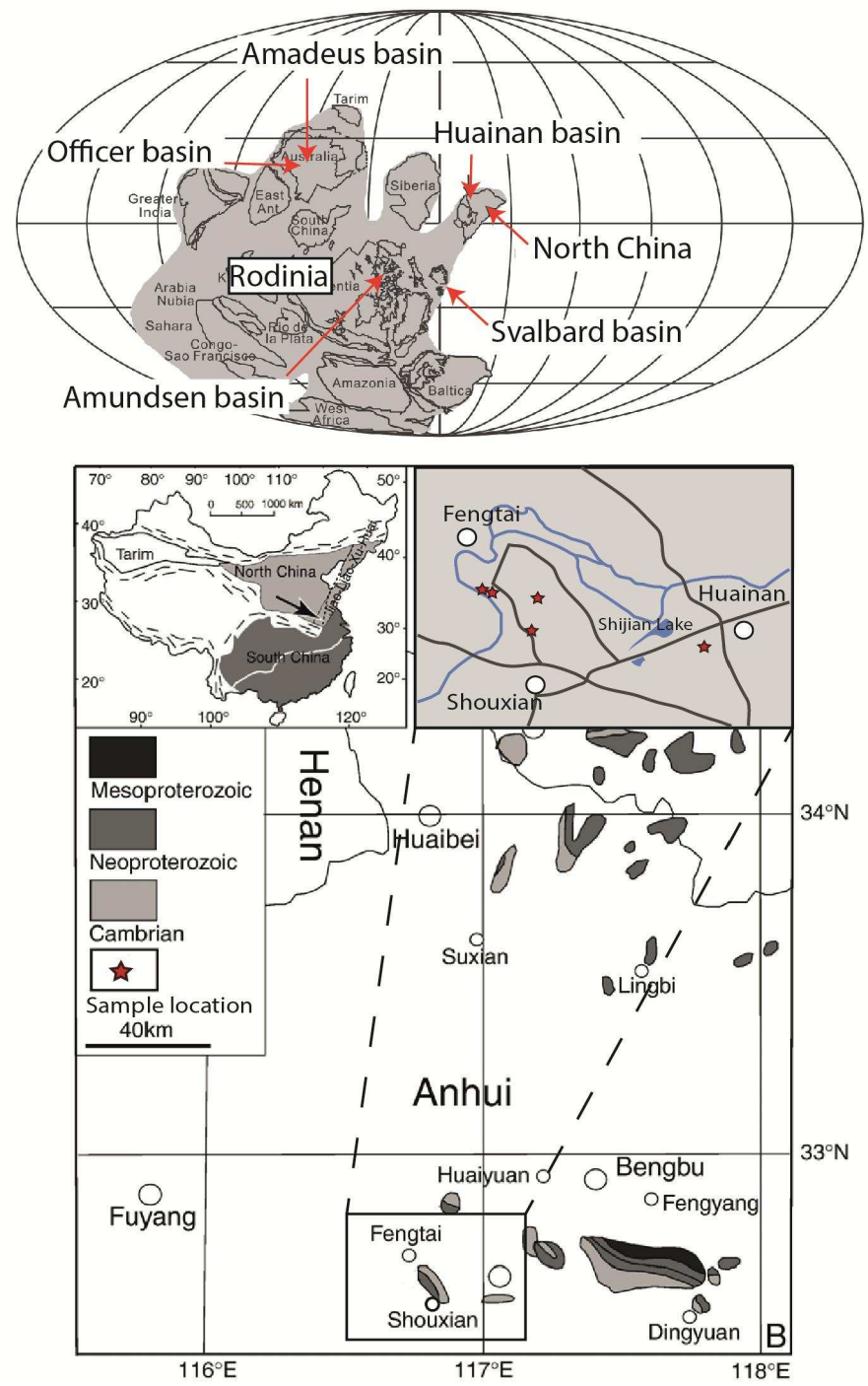

Fig. S1: Sample locations modified after Dong et al. (2008) and Tang et al. (2013). The upper part locates the study sites within the Rodinia supercontinent at ~900 Ma. The lower part shows the sample locations within the Huainan region (North China). Note that samples from the Amadeus, Amundsen, Officer and Spitsbergen basins are younger than 900 Ma, however their respective locations do not change substantially across this time interval.

~0.80 Ga Svanbergfjellet Formation, Svalbard basin, Spitsbergen

Spitsbergen samples consist of fresh, non-oxidised outcrops of shallow marine shales from the ~800 Ma [11] Svanbergfjellet Formation. Sample and acritarch assemblage descriptions have been detailed by Butterfield[12]. Fe_{Ox} contents do not show abnormal enrichments, suggesting limited sulphide oxidation.

~0.77 Ga Hussar and Kanpa Formations, Officer basin, Australia

Marine shales from the ~0.77 Ga Hussar and Kanpa formations have been collected from the unoxidised Munta-1 drillhole. Both formations yield distinctive *Cerebrosphaera* acritarchs[13,14].

Sulphur Isotope Data

Several lines of evidence suggest that S isotope data for both CAS and pyrite-S have not been affected by metamorphism or cross-contamination. All CAS data have been extracted from sediments with low Mn/Sr ratios, supporting negligible secondary remobilisation[15] (Mn/Sr < 10 for all samples). There is also no correlation between $\delta^{13}C_{carb}$ and $\delta^{18}O_{carb}$ (Fig. S2) that might imply significant post-early diagenetic overprinting[16]. Finally, there is no relationship between $\delta^{34}S_{CAS}$ and $\delta^{34}S_{pyrite}$, or between $\delta^{34}S_{CAS}$ and pyrite concentrations (Fig. S2), indicating that our data were not affected by authigenic carbonate formation or extensive pyrite oxidation[17]. Potential pyrite oxidation during CAS extraction may shift pristine $\delta^{34}S_{CAS}$ towards lower values. We are confident that our CAS extractions were not affected by pyrite oxidation (for which there is no evidence; see above discussion) since $\delta^{34}S_{CAS}$ is enriched in all of our samples, and some $\delta^{34}S_{pyrite}$ have preserved signatures > $\delta^{34}S_{CAS}$, as observed for other Neoproterozoic settings[18]. Potential atmospheric sulphate

contamination may also be a source of CAS-S isotope bias[19]. Peng et al.[19] analysed $\Delta^{17}O$ values in CAS from sub-humid regions in north central China exposed to anthropogenic sulphate from coal burning. Although it is possible that some of our samples were similarly affected, their findings suggest that <20% of CAS may have been contaminated. According to their model, this could not have shifted our CAS-S data by more than 2‰, which has no effect on our conclusions.

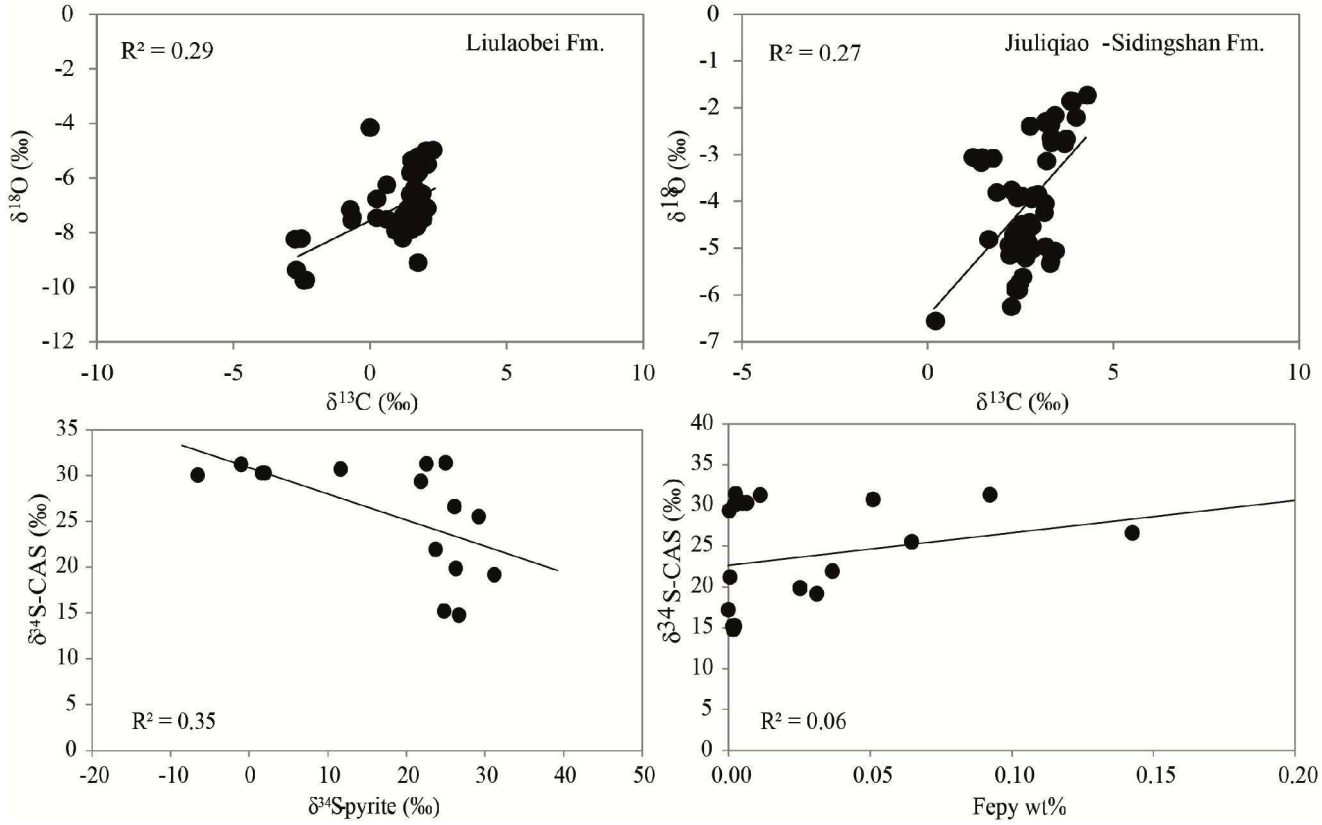

Fig. S2: Sulphur isotope quality checks for the Liulaobei Fm. and the conformable Jiuliqiao and Sidingshan Fms. The lack of correlation between $\delta^{18}O$ and $\delta^{13}C$ suggests insignificant burial diagenesis or meteoric alteration. The lack of correlation between $\delta^{34}S_{CAS}$ and $\delta^{34}S_{pyrite}$ and $\delta^{34}S_{CAS}$ and Fe_{py} (wt%) indicates that our dataset was not altered by carbonate authigenesis and pyrite oxiation.

Sulphur Isotope Systematics

The extent of S isotope fractionation between microbially derived sulphide and the sulphate source ($\Delta^{34}S$) is expressed by $\delta^{34}S_{Py}$ - $\delta^{34}S_{CAS}$. The magnitude of this fractionation depends upon several factors, including sulphate concentration, and

tends to ~0‰ when seawater sulphate is <1% of the modern value of 28 mM[20]. Fractionations observed throughout the Jiuliqiao and Sidingshan Formations (~23‰ on average, Fig. 1) are within the range of typical fractionations observed for sulphate concentrations of 0.2-1 mM[21]. $\delta^{34}S_{CAS} < \delta^{34}S_{Py}$ in the lower part of the section (Liulaobei Fm., Fig. 1), suggesting extremely low sulphate concentrations potentially affected by a series of Rayleigh-like fractionations during small extents of sulphide re-oxidation[18], or by minute amounts of secondary atmospheric contamination[19]. Both scenarios are suggestive of vanishingly low sulphate concentrations. The upper part of the Huainan basin (Jiuliqiao and Sidingshan Fms; Fig. 1) are characterised by high $\delta^{34}S_{CAS}$ which exhibits a remarkably small variation through time, whilst $\delta^{34}S_{Py}$ is also high and decreases towards the top of the section. ^{34}S enrichments in CAS and coeval pyrite suggest that a large proportion of seawater sulphate is removed from a small S reservoir as solid phase sulphide. The very low Fe_{Py} and CAS contents throughout the succession give further support to this assumption. In the upper part of the succession, the increase in $\Delta^{34}S$ is likely to be explained by increasing sulphate concentrations due to the proximity to continental sulphate input, allowing a more comprehensive expression of the fractionation associated with bacterial sulphate reduction. These data therefore give an estimate of maximum fractionations during deposition of the succession. A small degree of variability in $\delta^{34}S_{CAS}$ suggests steady state S cycling in the basin, and we integrated our results into a widely used S cycle box model at steady state[16,17,22], in order to estimate sulphate concentrations for the Jiuliqiao and Sidingshan basins.

Sulphur Cycle Box Model

In order to estimate seawater sulphate concentrations in the early Neoproterozoic we utilised a standard S-isotope box model. Variations in the amount of oceanic sulphate through time are given by the difference between total sulphur input fluxes and sulphur removal fluxes (Eq. S1):

$$\frac{\partial M_0}{\partial t} = F_W + F_V + F_M - (F_{Py} + F_{Evap}) \qquad \text{Eq. S1}$$

where M_0 is the amount of sulphate-S in the ocean (mol), F_W (mol/Ma) is the S input flux to the ocean from continental weathering, F_V (mol/Ma) is the volcanic S input flux to the ocean, F_M (mol/Ma) is the hydrothermal S input flux, F_{Py} (mol/Ma) is the pyrite burial flux and F_{Evap} (mol/Ma) is the evaporitic and carbonate-associated burial flux. Multiplying each member by its isotopic composition, variations in the S isotope composition of the ocean reservoir through time ($d\delta_0/dt$ in ‰/Ma) can be expressed by (Eq. S2):

$$\frac{d\delta_0}{dt} = \frac{F_W\delta_W + F_V\delta_V + F_M\delta_M - (F_W + F_V + F_M)\delta_0 - F_{Py}\Delta S}{M_0} \qquad \text{Eq. S2}$$

where δ is the isotope composition of each flux (in ‰) and ΔS is the S isotope fractionation between sulphide and sulphate phases ($\delta_{Py} - \delta_0$ in ‰).

Input parameters are summarised in Table S2 (modern input parameters and associated isotope compositions are from ref [17]. Sedimentation rates are poorly constrained for the ~200 m thick sediments studied here, and three different estimates for $d\delta_0/dt$ were explored using various deposition rates (10, 20 and 40 m/Ma). We assumed that our δ_{CAS} data are reflective of the isotopic composition of seawater sulphate, δ_0. For δ_{Py}, we took different average points to best represent the temporal trend in δ_{Py} and account for moderate spatial variability (Fig. 1). ΔS was taken as the

difference between δ_{Py} and δ_0. However, at the bottom of the Jiuliqiao Formation where δ_{Py} approaches δ_0, apparent ΔS may be biased by Rayleigh-like fractionations and we assumed that ΔS was effectively similar to the rest of the succession where the full expression of ΔS is recorded (26.3‰).

For the input and output S fluxes and their associated isotope composition, three different scenarios were tested against modern estimates (Table S2). The hydrothermal S flux and its isotopic composition (F_M, δ_M) were assumed to approximate modern values[17]. For F_V, we used the lower estimate of modern fluxes[23,24] to account for restricted volcanic degassing on the Rodinia supercontinent, and δ_M was assumed to approximate modern values. We varied the weathering flux F_W in the three different scenarios to explore the impact of changes in weathering fluxes on a low latitude supercontinent. In scenario 1, the S weathering flux was 1.5 times the modern value. In scenario 2, F_W was 0.5 times the modern value. In scenario 3, F_W was 0.067 times the modern value. This 15 fold decrease in this S influx to the open ocean accounts for the increase in continental evaporitic deposits on Rodinia, as suggested by a ~15 times increase in the magnitude of sulphate-rich evaporite deposition in the early Neoproterozoic[25]. Peneplanation of Rodinia and the drop in crustal reworking[26] may have further diminished the S weathering flux to the ocean. Abundant anhydrite and gypsum pseudomorphs associated with this increase in evaporitic deposition have been reported[27,28], in contrast to the halite-dominated record of the largest previous evaporitic basin (~1.87 Ga Stark Formation) where gypsum and anhydrite pseudomorphs are exceptionally rare, if observed at all[29].

Sulphate removal as continental evaporites records the isotope composition of the source, δ_W, as opposed to δ_0. The isotopic composition of the weathering flux (δ_W) has been explored for different proportions of weathered materials (*i.e.* evaporites, shales, and volcanic rocks). We used estimates of seawater sulphate isotope composition[30] at 1 Ga (~20‰) for the isotope composition of weathered evaporites, the average isotope composition of pyrite for the early Neoproterozoic[24] (~5‰) for the isotope composition of weathered shales, and modern values for weathered volcanic rocks[17] (3‰). Varying the proportion of the evaporitic source from 10 to 40% of the total S influx resulted in a ~5–11‰ range of potential δ_W, and our model explored δ_W values of 6, 8 and 10‰ in order to reflect this potential variability.

At steady state, the sum of output fluxes balances the sum of input fluxes (*i.e.* $F_{Py} + F_{Evap} = F_W + F_V + F_M$). Our isotope data ($^{34}S$ enriched pyrite) suggest that the vast majority of S was removed as pyrite in the basin. F_{Evap} was set to match mass balance. In both scenario 1 and 2, F_{Py} overwhelms the modern value, whereas it is quite clear that pyrite contents in our study are below the modern average mudstone content[31]. Scenario 3, which extensively reduces F_W through evaporite deposition on Rodinia, allows F_{Py} to agree with the observations that i) pyrite contents are ~2 times lower than in the modern environment, and ii) the pyrite burial flux accounts for most of the S removal mechanism in the basin. Sensitivity tests on δ_W and deposition rates are illustrated by Fig. S3. The range of potential δ_W and deposition rates are unlikely to cause the extremely large variations in seawater sulphate concentrations observed in scenarios 1 and 2. Scenario 3 allows seawater sulphate concentrations to vary as a function of δ_W and different deposition rates in a more realistic way. Using a δ_W of 8‰ as suggested for the Neoproterozoic[16] and the Cambrian[22] and a deposition rate of

40 m/My (averaging the values used by ref. [32]) leads to seawater sulphate concentrations of 0.8 ± 0.2 mM on average (scenario 3), which represents our best estimate of seawater sulphate concentration.

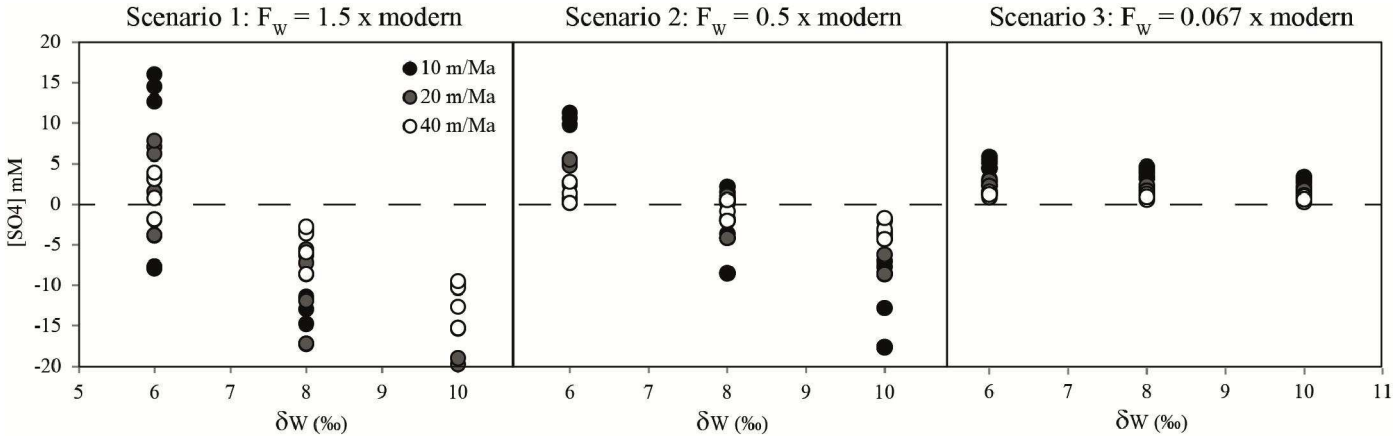

Fig. S3: Sensitivity tests for deposition rates and δ_W explored for the three F_W scenarios. All other parameters are set as described in the text and summarised in Table S2. Note that scenario 1 displays [SO_4] values << -20 mM (out of axis on the figure). Plausible sulphate concentrations (i.e. positive values), are obtained when F_W is reduced substantially (scenario 3).

We integrated our results from scenario 3 into the estimated curve for seawater sulphate evolution through the Proterozoic[32]. Kah et al.[32] used our lower estimate for δ_W (6‰) and deposition rates averaging 40 m/My (which corresponds to our upper estimate) in order to reconstruct maximum seawater sulphate concentrations using a simplification of Eq. S2 (Eq. S3):

$$\frac{d\delta_{\max}}{dt} = \frac{-F_W \Delta S}{M_{\max}} \qquad \text{Eq. S3}$$

where $d\delta_{max}/dt$ is the maximum rate of isotopic change of seawater sulphate M_{max}. Our estimates on Fig. 3 (red oval) also include calculations using Eq. S3 in order to be consistent with the Kah et al.[32] approach.

References:

1. Dong, L. *et al.* Restudy of the worm-like carbonaceous compression fossils Protoarenicola, Pararenicola, and Sinosabellidites from early Neoproterozoic successions in North China. *Palaeogeography, Palaeoclimatology, Palaeoecology* **258,** 138–161 (2008).
2. Tang, Q. *et al.* Organic-walled microfossils from the early Neoproterozoic Liulaobei Formation in the Huainan region of North China and their biostratigraphic significance. *Precambrian Research* **236,** 157–181 (2013).
3. Wang, G. *et al.* Research on the upper Precambrian of northern Jiangsu and Anhui Provinces. *Hefei: Anhui Press of Science and Technology* (1984).
4. Liu, Y., Gao, L., Liu, Y., Song, B. & Wang, Z. Zircon U-Pb dating for the earliest Neoproterozoic mafic magmatism in the southern margin of the North China Block. *Chinese Science Bulletin* **51,** 2375–2382 (2006).
5. Yang, D.-B. *et al.* U–Pb ages and Hf isotope data from detrital zircons in the Neoproterozoic sandstones of northern Jiangsu and southern Liaoning Provinces, China: Implications for the Late Precambrian evolution of the southeastern North China Craton. *Precambrian Research* **216–219,** 162–176 (2012).
6. Xiao, S. *et al.* Biostratigraphic and chemostratigraphic constraints on the age of early Neoproterozoic carbonate successions in North China. *Precambrian Research* (2014). doi:10.1016/j.precamres.2014.03.004
7. Yang, J., Zheng, W., Wang, Z. & Tao, X. Age determining of the Upper Precambrian system of northern Jiangsu-Anhui by using Sr and C isotopes. *Journal of Stratigraphy* **25,** 44–47 (2001).
8. Thomson, D., Rainbird, R. H. & Dix, G. Architecture of a Neoproterozoic intracratonic carbonate ramp succession: Wynniatt Formation, Amundsen Basin, Arctic Canada. *Sedimentary Geology* **299,** 119–138 (2014).
9. Butterfield, N. J. Probable proterozoic fungi. *Paleobiology* **31,** 165–182 (2005).
10. Swanson-Hysell, N. L. *et al.* Cryogenian glaciation and the onset of carbon-isotope decoupling. *Science* **328,** 608–611 (2010).
11. Halverson, G. P., Maloof, A. C., Schrag, D. P., Dudás, F. Ö. & Hurtgen, M. Stratigraphy and geochemistry of a ca 800 Ma negative carbon isotope interval in northeastern Svalbard. *Chemical Geology* **237,** 5–27 (2007).
12. Butterfield, N. J. A vaucheriacean alga from the middle Neoproterozoic of Spitsbergen: implications for the evolution of Proterozoic eukaryotes and the Cambrian explosion. *Paleobiology* **30,** 231–252 (2004).
13. Cotter, K. L. Microfossils from Neoproterozoic Supersequence 1 of the Officer Basin, Western Australia. *Alcheringa* **23,** 63–86 (1999).
14. Hill, A. & Walter, M. Mid-Neoproterozoic (~ 830–750 Ma) isotope stratigraphy of Australia and global correlation. *Precambrian Research* **100,** 181–211 (2000).
15. Kaufman, A. J. & Knoll, A. H. Neoproterozoic variations in the C-isotopic composition of seawater: stratigraphic and biogeochemical implications. *Precambrian Research* **73,** 27–49 (1995).
16. Loyd, S. J. *et al.* Sustained low marine sulfate concentrations from the Neoproterozoic to the Cambrian: Insights from carbonates of northwestern Mexico and eastern California. *Earth and Planetary Science Letters* **339,** 79–94 (2012).
17. Adams, D. D., Hurtgen, M. T. & Sageman, B. B. Volcanic triggering of a biogeochemical cascade during Oceanic Anoxic Event 2. *Nature Geoscience* **3,** 201–204 (2010).

18. Ries, J. B., Fike, D. A., Pratt, L. M., Lyons, T. W. & Grotzinger, J. P. Superheavy pyrite (δ34Spyr> δ34SCAS) in the terminal Proterozoic Nama Group, southern Namibia: A consequence of low seawater sulfate at the dawn of animal life. *Geology* **37,** 743–746 (2009).
19. Peng, Y. *et al.* Widespread contamination of carbonate-associated sulfate by present-day secondary atmospheric sulfate: Evidence from triple oxygen isotopes. *Geology* (2014). doi:10.1130/G35852.1
20. Habicht, K. S., Gade, M., Thamdrup, B., Berg, P. & Canfield, D. E. Calibration of Sulfate Levels in the Archean Ocean. *Science* **298,** 2372 –2374 (2002).
21. Canfield, D. E., Farquhar, J. & Zerkle, A. L. High isotope fractionations during sulfate reduction in a low-sulfate euxinic ocean analog. *Geology* **38,** 415–418 (2010).
22. Gill, B. C. *et al.* Geochemical evidence for widespread euxinia in the Later Cambrian ocean. *Nature* **469,** 80–83 (2011).
23. Stoiber, R. E., Williams, S. N. & Huebert, B. Annual contribution of sulfur dioxide to the atmosphere by volcanoes. *Journal of Volcanology and Geothermal Research* **33,** 1–8 (1987).
24. Canfield, D. E. The evolution of the Earth surface sulfur reservoir. *Am J Sci* **304,** 839–861 (2004).
25. Evans, D. A. D. Proterozoic low orbital obliquity and axial-dipolar geomagnetic field from evaporite palaeolatitudes. *Nature* **444,** 51–55 (2006).
26. Spencer, C. J. *et al.* Proterozoic onset of crustal reworking and collisional tectonics: Reappraisal of the zircon oxygen isotope record. *Geology* **42,** 451–454 (2014).
27. Walter, M., Veevers, J., Calver, C. & Grey, K. Neoproterozoic stratigraphy of the Centralian Superbasin, Australia. *Precambrian Research* **73,** 173–195 (1995).
28. Spear, N. *et al.* Analyses of fluid inclusions in Neoproterozoic marine halite provide oldest measurement of seawater chemistry. *Geology* **42,** 103–106 (2014).
29. Pope, M. C. & Grotzinger, J. P. Paleoproterozoic stark formation, Athapuscow Basin, Northwest Canada: record of cratonic-scale salinity crisis. *Journal of Sedimentary Research* **73,** 280–295 (2003).
30. Canfield, D. E. Biogeochemistry of Sulfur Isotopes. *Reviews in Mineralogy and Geochemistry* **43,** 607–636 (2001).
31. Berner, R. A. Burial of organic carbon and pyrite sulfur in the modern ocean; its geochemical and environmental significance. *Am. J. Sci.* **282,** 451–473 (1982).
32. Kah, L. C., Lyons, T. W. & Frank, T. D. Low marine sulphate and protracted oxygenation of the Proterozoic biosphere. *Nature* **431,** 834–838 (2004).